Available online at www.sciencedirect.com
ScienceDirect
Trans. Nonferrous Met. Soc. China 35(2025) 3507−3519
Transactions of Nonferrous Metals Society of China
www.tnmsc.cn

Erosion and diffusion kinetics of PbTe in selenium melts

Lang LIU[1,2,3], Ji-lin HE[4], Xian-jun LEI[1,2,3,5], Huan LUO[1,2,3], Guo-zheng ZHA[1,2,3,5], Ru-yi JI[6], Wen-long JIANG[1,2,3,5], Bin YANG[1,2,3,5], Bao-qiang XU[1,2,3,5]

1. Key Laboratory for Nonferrous Metals Vacuum Metallurgy of Yunnan Province, Kunming University of Science and Technology, Kunming 650093, China;
2. National Engineering Research Center of Vacuum Metallurgy, Kunming University of Science and Technology, Kunming 650093, China;
3. Faculty of Metallurgical and Energy Engineering, Kunming University of Science and Technology, Kunming 650093, China;
4. College of Materials Science and Engineering, Zhengzhou University, Zhengzhou 450001, China;
5. State Key Laboratory of Complex Non-ferrous Metal Resources Clean Utilization, Kunming University of Science and Technology, Kunming 650093, China;
6. College of Materials Science and Engineering, Sichuan University, Chengdu 610064, China

Received 4 January 2024; accepted 2 August 2024

Abstract: The erosion process and kinetics of PbTe particles in a selenium melt were investigated. The results reveal that the limiting step of the reaction is controlled by product layer diffusion and the interfacial chemical reaction at low temperatures (573, 583, and 593 K), but the limiting step is controlled by boundary layer diffusion at high temperatures (603 and 613 K). The Se- and Te-atom diffusion in the product layer becomes unbalanced as the product layer thickens, with Kirkendall voids generating in the product layer accelerating PbTe particle erosion. After the PbTe impurities in the selenium melt evolve into PbSe and Te, Te is evenly distributed in the selenium melt owing to the solubility of Se and Te. This study serves to clarify the evolution behavior of PbTe impurities in the selenium melt and the reason that Te often occurs in Se.

Key words: PbTe; selenium; diffusion kinetics; erosion behavior

1 Introduction

Selenium, which is a rare metal with exceptional physicochemical properties, is used extensively in metallurgical, materials, chemical, agricultural, and medical fields. The advent of new selenium-containing materials and the surge in selenium-enriched agricultural products have led to an escalating demand for selenium in the atomic energy [1], solar energy [2], semiconductor [3], food [4], and health sectors [5]. Consequently, high-purity selenium has emerged as a crucial raw material for the advancement of technology and the development of novel materials. However, the scarcity of Se in the Earth's crust poses a significant challenge. Approximately 90% of Se is extracted through comprehensive recovery from electrolytic copper anode sludge [6,7]. Removing impurities such as tellurium and lead is a major obstacle to the production of high-purity selenium. In recent years, several methods have been used to eliminate impurities from crude selenium, including those that rely on the redox reactions [8], leaching [9,10],

Corresponding author: Bao-qiang XU, Tel: +86-13608864121, E-mail: kmxbq@126.com
https://doi.org/10.1016/S1003-6326(25)66896-8

and solvent extraction [11]. Although these methods have yielded promising results, they often consume substantial amounts of solvent and generate toxic and hazardous substances.

Vacuum distillation has emerged as a promising low-energy metallurgical technique for the efficient separation of metals [12]. This process has recently attracted considerable attention for the purification of selenium. MEI et al [13] applied primary distillation to 91%-pure crude selenium and obtained 98.91%-pure selenium product, albeit with a high content (0.63%) of Te impurities. Purifying selenium by vacuum distillation is highly selective for raw materials owing to the various forms of elemental impurities present in crude selenium. Impurity elements, such as Te and Pb, are not only present in their elemental states but also in the forms of PbTe and PbSe [14,15]. It is difficult to achieve a good separation of Se and elemental Te impurities by vacuum distillation owing to the complete mutual solubility of Se and Te. Se and Te easily form a eutectic system, and the Se−Te system exhibits an azeotropic phenomenon [16]. The abovementioned impurities volatilize in the Se gas phase during vacuum distillation and condense with Se, and thus these impurities are crucial factors that influence the purity of the distilled Se product. Therefore, investigating the behavioral characteristics of the impurity components in crude Se is important. While LUO et al [7,17] studied the volatilization characteristics and decomposition behavior of PbTe and PbSe impurities under vacuum conditions, less research has been reported on the evolutionary behavior of these impurities in the Se melt. Our recent studies revealed that PbTe evolves into PbSe and Te when crude selenium is melted. However, the specific evolution process of the PbTe impurity remain unknown.

In this study, we observe and investigate the erosion behavior of PbTe particles in a selenium melt. The results of this study are expected to clarify the presence of PbTe and Te in selenium and facilitate the development of an efficient selenium purification process.

2 Experimental

2.1 Materials

High-purity selenium particles (~99.999 wt.%) were obtained from the Chengdu CNBM Opto-electronic Materials Co., Ltd., China; PbTe (~99.999 wt.%) was sourced from the Hangzhou Kaiyada Semiconductor Materials Co., China. The chemical compositions of the two materials are listed in Tables 1 and 2, respectively, indicating that both Se and PbTe contain minimal impurities that are expected to negligibly impact the experimental results. The PbTe material used in the experiments was sieved to obtain irregularly shaped particles less than 150 μm in size. These particles were subsequently compressed using a tablet press to form cylindrical samples with a length of 5 mm and diameter of 3 mm.

2.2 Experimental methods

The behavior and reaction mechanism of PbTe impurity particles in a selenium melt were investigated. First, a selenium sample (3 g) was weighed and placed in a corundum crucible with a diameter of 12 mm. The crucible was then carefully positioned in the heating device and gradually heated at 10 K/min to a steady temperature of 583 K, which was maintained for 15 min to ensure that the selenium was melted completely. The corundum crucible was subsequently removed from the heating device and cylindrical PbTe particles with a diameter of 3 mm were swiftly introduced into the molten selenium. The corundum crucible containing the selenium and PbTe particles was then returned to the heating device for further thermal treatment. The corundum crucible was heated to various temperatures (573, 583, 593, 603,

Table 1 Chemical composition of PbTe (10^{-4} wt.%)

Co	Ag	Cu	Al	Mg	Ni	In	Sn	Fe	As	PbTe
≤0.1	≤0.2	≤0.5	≤0.5	≤0.5	≤0.5	≤0.5	≤1.0	≤0.5	≤0.5	Bal.

Table 2 Chemical composition of high-purity Se (10^{-4} wt.%)

Cu	Ag	Mg	Ni	Bi	In	Fe	Cd	Te	Al	Ti	Pb	Hg	Sb	Se
≤0.2	≤0.2	≤0.5	≤0.2	≤0.5	≤0.5	≤0.5	≤0.2	≤1	≤0.5	≤0.5	≤0.5	≤1	≤0.5	Bal.

and 613 K) for 10, 20, 30, 40, 50, and 60 min. This stepwise temperature increase enabled the reaction between the PbTe impurity particles and the selenium melt to be investigated in a controlled manner. After the desired thermal treatment, the crucible was removed from the heating device and allowed to cool in water. A schematic of the heating device used in the experiment is shown in Fig. 1.

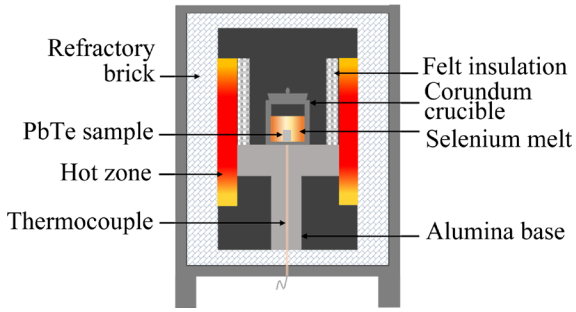

Fig. 1 Schematic diagram of experimental apparatus

The reaction mechanism associated with the behavior of PbTe in the selenium melt was investigated through a series of carefully executed steps at the end of the experiment. The corundum crucible containing the sample was quenched rapidly and cooled to ensure that the composition of the product layer at room temperature accurately reflected that under experimental conditions. The corundum crucible was subsequently meticulously sliced using a diamond wire cutter to extract the sample, which was then radially sectioned, embedded in epoxy resin, and subjected to a sequence of sanding and polishing steps to prepare for analysis. Scanning electron microscopy (SEM) augmented with energy dispersive X-ray spectroscopy (EDS) was used to characterize the product layer. The obtained SEM images were further analyzed using Fiji image-processing software to determine the thickness of the product layer. In addition, the characteristics of the product layer were examined using EDS. The erosion rate (R) of the PbTe particles in the selenium melt was calculated using Eq. (1):

$$R=\frac{d}{t} \tag{1}$$

where d is the depth of PbTe particles eroded by selenium melt (μm), and t is the erosion time (min).

2.3 Characterization

A micro-area X-ray diffractometer (Micro-area XRD; Mini-Flex 600, Japan) was used to characterize the areal phases of the samples over scanning angles (2θ) of 10°−90° at a scan rate of 5 (°)/min. The microscopic morphologies of the PbTe in the various samples were characterized by SEM. EDS was used to examine the distributions of Se, Te, and Pb at the interfaces between the PbTe particles and the selenium melt using an electron probe microanalyzer (EPMA; JXA8230, JEOL, Japan) at an accelerator voltage of 20 kV and a beam current of 2×10^{-9} A. The Gibbs free energy of the reaction was calculated using the "Reaction Equations" module of HSC Chemical 6.0.

3 Results and discussion

3.1 PbTe-particle behavior in selenium melt

3.1.1 Erosion process

The Gibbs free energy changes (ΔG) associated with the reaction between Se and PbTe at different temperatures were calculated, revealing that ΔG is negative for this reaction in the temperature range of 300−700 K. The relevant reaction is represented as follows:

$$Se+PbTe=PbSe+Te \tag{2}$$

Selenium typically melts between 493 and 693 K. The calculated ΔG values clearly reveal that the thermodynamic conditions necessary for the reaction to proceed are met within the temperature range associated with this Se phase transition.

Figure 2 shows cross-sectional microstructural images of the various samples obtained following PbTe particle erosion in a selenium melt at 593 K for 20 min. Distinct reactant and product layers are clearly visible in Fig. 2(a); the bright white region on the left corresponds to the PbTe phase, while the light gray region in the middle primarily corresponds to the PbSe phase, and the dark gray region on the right corresponds to Se. These observations are consistent with the micro-area XRD results shown in Figs. 3(a, b) for the reactant and product layers, respectively. Elemental Se, Te, and Pb maps showing the surface distributions are presented in Figs. 2(b−d), respectively, and reveal evident Se and Te concentration gradients in the product layer. Figure 2(e) shows EDS-determined Se, Te, and Pb concentration

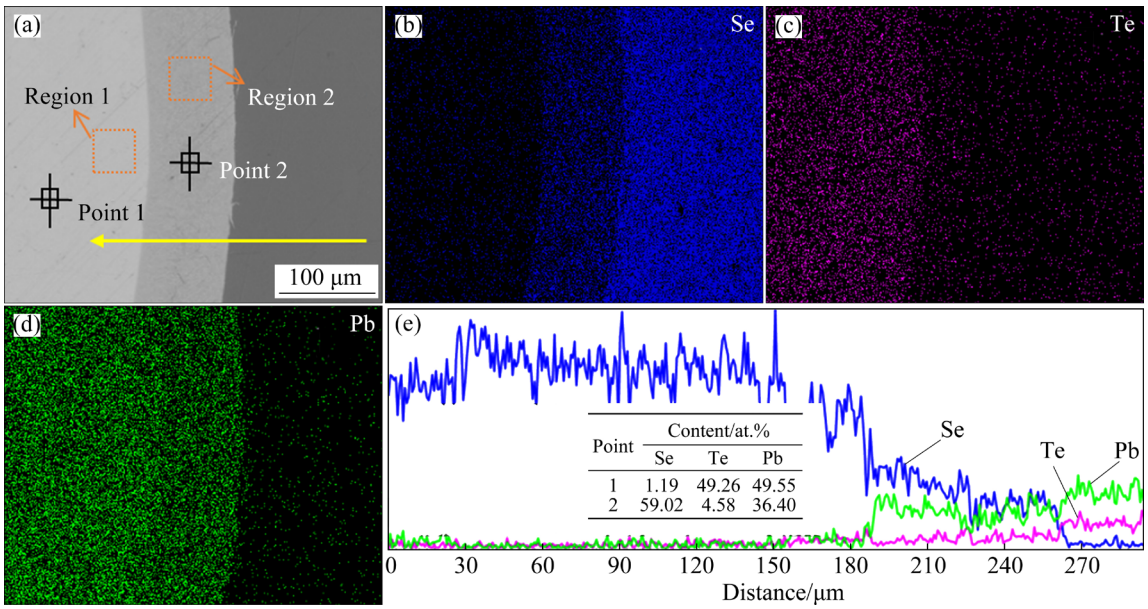

Fig. 2 Micrographs of reactive and product layers of PbTe particles after 20 min of erosion in selenium melt at 593 K: (a) SEM-BSE image; (b−d) Se, Te, and Pb elemental EDS maps, respectively; (e) EDS line scans along yellow line in (a) along with point data

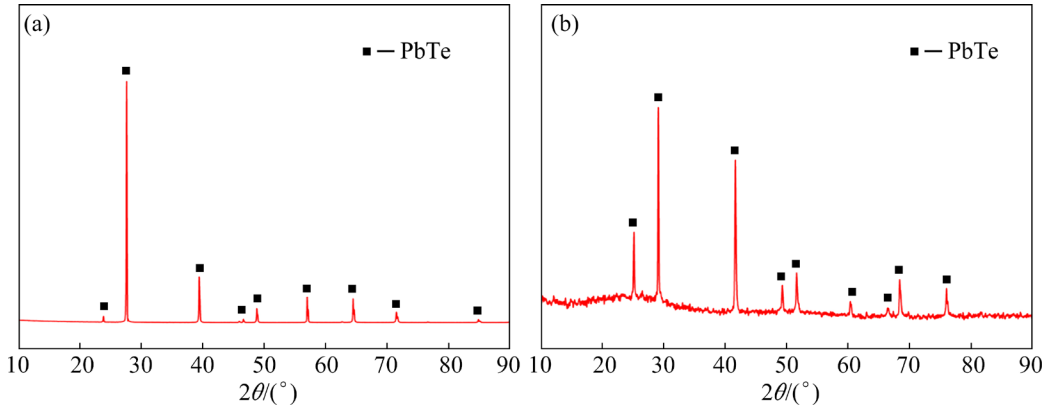

Fig. 3 Micro-area XRD patterns of Regions 1 (a) and 2 (b) in Fig. 2(a)

distributions at different positions in the interface. The concentration of Se within the PbTe particles and that of Te within the selenium melt change during the erosion process because Se is initially absent from the PbTe particles while Te is not initially present in the selenium melt. Therefore, the Se and Te concentration distributions can be used to reveal the reaction behavior of PbTe particles eroded by the selenium melt.

Figure 4 shows the microstructures of the interfaces and the corresponding Se, Te, and Pb elemental line-scans of PbTe particles immersed in the selenium melt at 583 K for various durations. The boundary contours of the product layers within the interfacial regions are clearly visible in Figs. 4(a, c, e, g, i, k). However, the solid-phase boundary layer between the product layer and PbTe particles, and the liquid-phase boundary layer between the product layer and the selenium melt, are not distinct. The line-scan analysis along the direction indicated by the yellow arrow shows two distinct steps in the middle of each curve, consistent with the formation of new phases; the thicknesses of the product and boundary layers can be determined from the distances between these steps. Analysis of the line-scan data reveals that the concentrations of elemental Se and Pb in the product layer remain relatively stable, with a concentration ratio close to 1:1, which suggests that PbSe is generated within the product layer, consistent with the results presented in Fig. 3.

A liquid boundary layer is observed at the

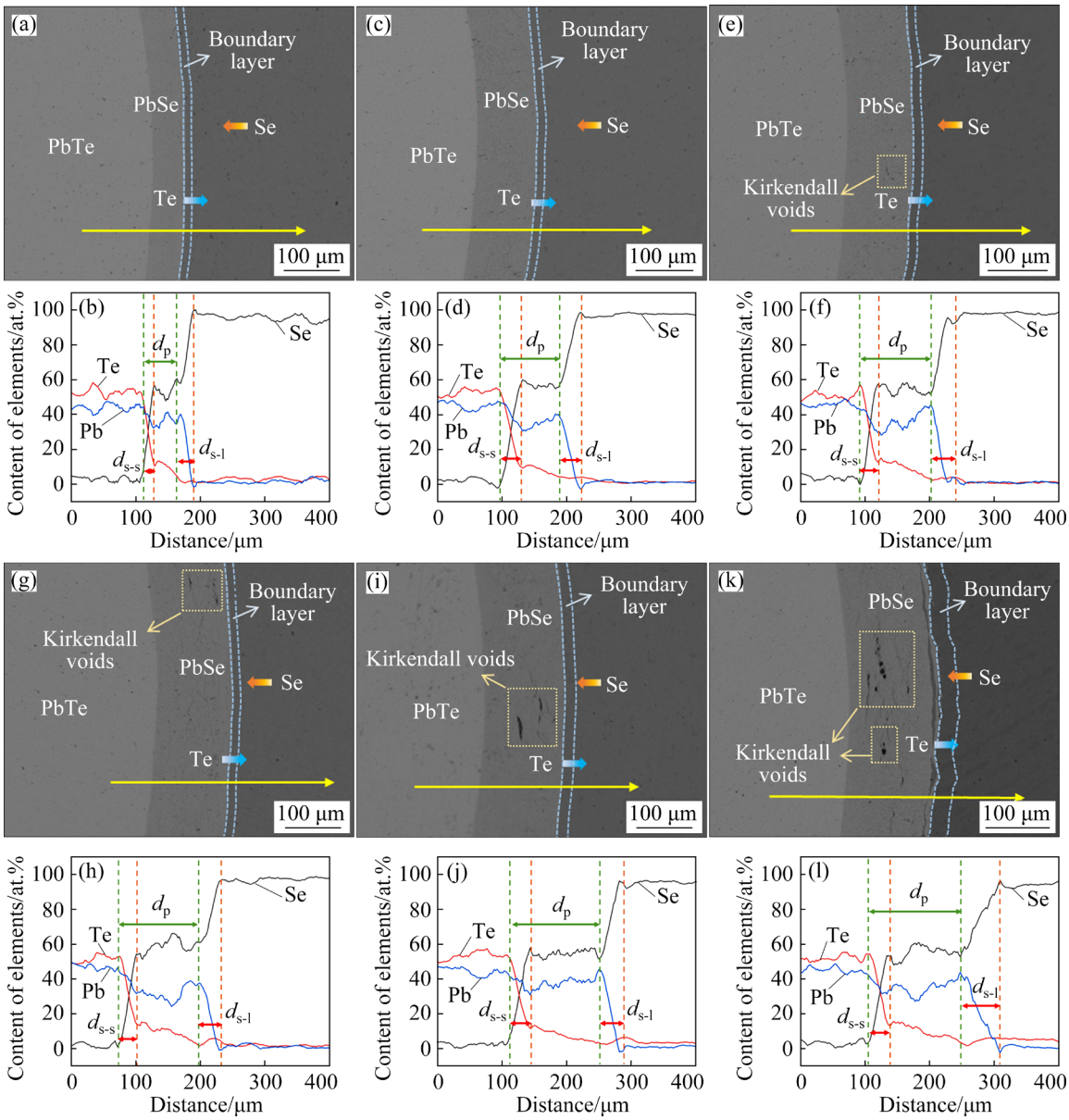

Fig. 4 Microstructures of interfacial regions at 583 K (a, c, e, g, i, k) and corresponding Se, Te, and Pb line-scan analyses along yellow directional arrows (b, d, f, h, j, l) for different erosion time: (a, b) 10 min; (c, d) 20 min; (e, f) 30 min; (g, h) 40 min; (i, j) 50 min; (k, l) 60 min

interface between the product layer and the selenium melt. The concentrations of Te in the product and liquid boundary layers gradually decrease from the PbTe particle boundary to the selenium melt, indicative of Te diffusion within the product and boundary layers. The green dashed lines (d_p) in Figs. 4(b, d, f, h, j, l) demarcate the product layer and PbTe reactant layer, as well as the liquid boundary layer, while the orange dashed lines demarcate the solid-phase boundary layer within the product and the liquid-phase boundary layer within the selenium melt. The spacing between the two green dashed lines indicates the thickness of the product layer, whereas the spacing between the green and orange dashed lines shows the thickness of the solid-phase boundary layer (d_{s-s}) and liquid-phase boundary layer (d_{s-l}), respectively. The PbTe particles immersed in the selenium melt undergo evident erosion, resulting in the formation of PbSe and Te. PbSe forms a solid product layer that encapsulates the internal PbTe particles. The generated Te atoms diffuse into the selenium melt through the product and boundary layers owing to the infinite mutual solubility of Te in Se. The product layer thickens with increasing reaction time at a reaction temperature of 583 K; additionally, a

few voids and cracks begin to appear on the outer surface of the product layer with increasing reaction time.

Figure 5 shows microstructural and corresponding line-scan images for Se, Te, and Pb at the interfaces of PbTe particles reacted in a selenium melt for 20 min at various temperatures. Figures 5(a, c, e, g, i) show that the product layer gradually thickens with increasing reaction temperature after reacting for 20 min. Furthermore, the product layer exhibits voids and cracks when reacting at 593 K, and some PbSe is exfoliated from the product layer and dispersed in the surrounding selenium melt. Both the number and sizes of voids increase significantly as the temperature is further increased to 613 K. In addition, the number of cracks on the outer side of the product layer increases; these cracks are subsequently filled with the selenium melt. The line-scan data presented in Figs. 5(b, d, f, h, j) clearly show the steps formed by the product and boundary layers. The distance, d_p, between the two green dotted lines closely corresponds to the thickness of the product layer, as measured using Fiji image-processing software. The thickness of the product layer is measured at different temperatures and reaction times, as summarized in Table 3.

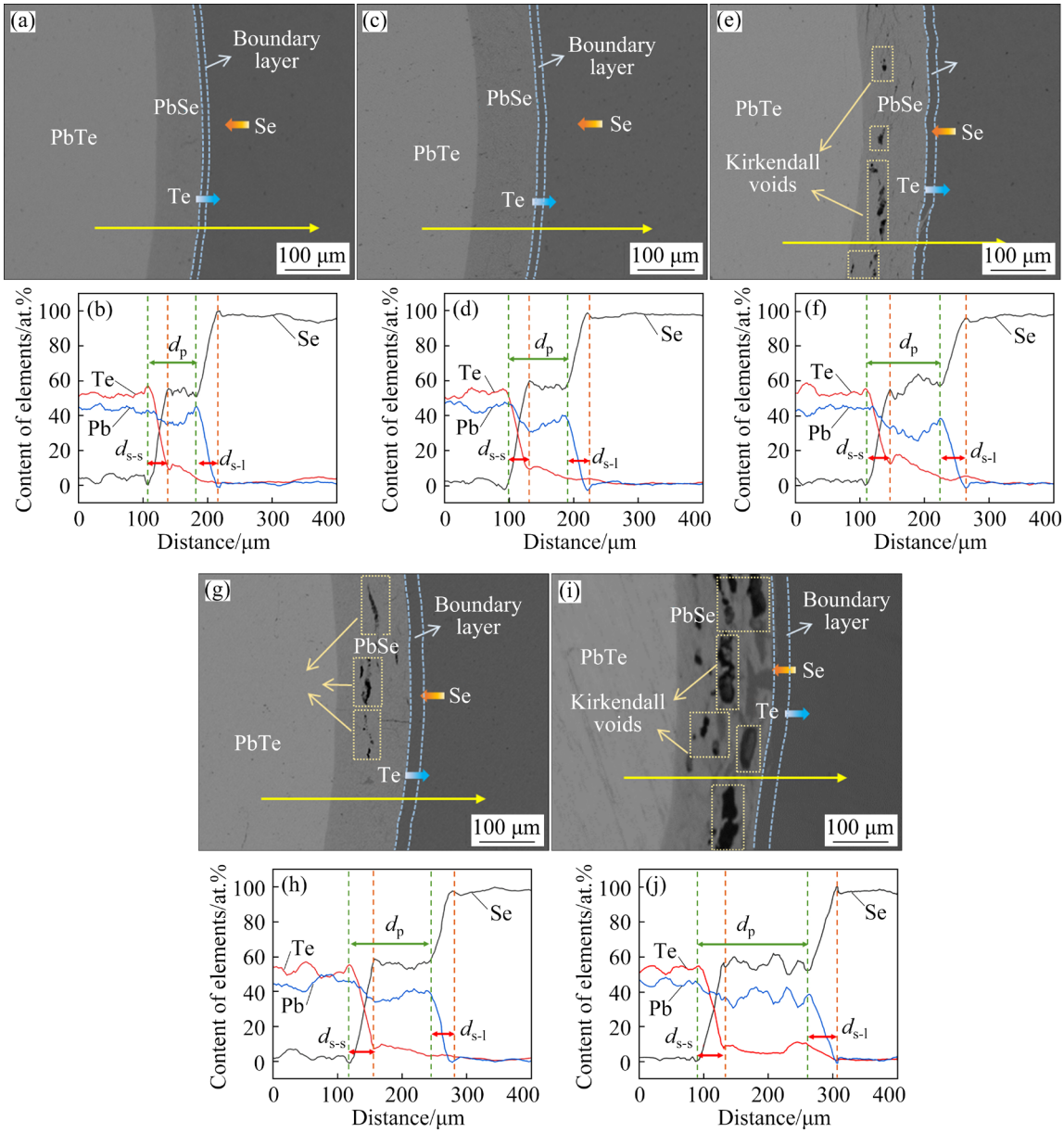

Fig. 5 Microstructures of interfacial regions (a, c, e, g, i) and corresponding Se, Te, and Pb line-scan analyses along yellow directional arrows (b, d, f, h, j) after reaction for 20 min at various temperatures: (a, b) 573 K; (c, d) 583 K; (e, f) 593 K; (g, h) 603 K; (i, j) 613 K

Table 3 Product-layer thickness at different temperatures and different reaction time

Temperature/K	Product-layer thickness/μm					
	10 min	20 min	30 min	40 min	50 min	60 min
573	44.92	71.19	92.69	108.71	112.34	124.80
583	59.86	103.17	112.43	121.92	132.23	143.19
593	73.03	112.16	148.43	164.41	185.54	212.56
603	82.35	134.73	192.82	281.08	336.72	440.11
613	91.48	164.36	244.82	418.32	630.85	927.33

3.1.2 Influencing factors

The temperature and reaction time are the primary factors that influence the PbTe particle erosion rate in a selenium melt. Figure 6 shows the relationships among the product layer thickness, temperature, and reaction time, measured every 10 min, which shows that the product layer gradually thickens with increasing temperature and reaction time. The product layer is observed to thicken more rapidly during the initial 30 min and then plateau after 30 min at 573, 583, and 593 K; in contrast, it continues to thicken with increasing reaction time at 603 and 613 K. Figure 7 shows the impact of the temperature and reaction time on the PbTe particles, as represented by the average rate per 10 min.

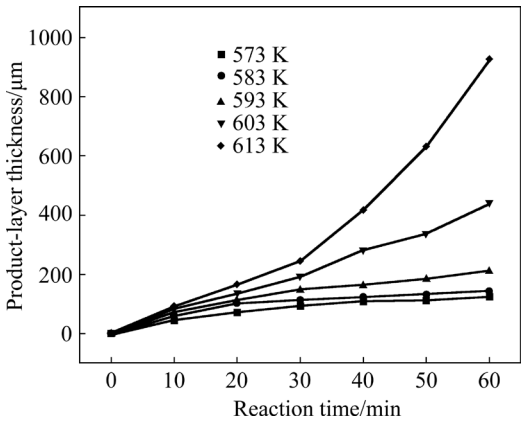

Fig. 6 Product layer thickness as function of temperature and reaction time

Temperature plays a significant role in the erosion rate of the PbTe particles in the selenium melt. The results show that the reaction rate increases with increasing temperature, with notable accelerations observed at 603 and 613 K. The following relationship between diffusion coefficient (D), viscosity (u), and temperature (T) can be obtained from the Stokes–Einstein equation [18,19]:

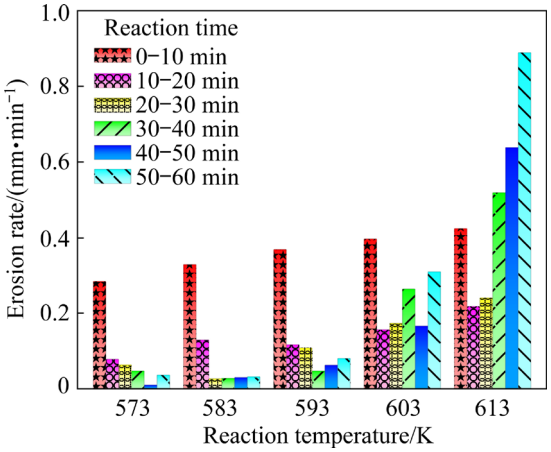

Fig. 7 Effects of reaction temperature and reaction time on erosion rate of PbTe particles in selenium melt

$$D = \frac{k_B T}{6\pi u r'} \tag{3}$$

where r' represents the radius of the diffusion phase, and k_B is the Boltzmann constant. According to this equation, an increase in temperature leads to an increase in the diffusion coefficient. Furthermore, an increase in temperature reduces the viscosity of the selenium melt, thus further improving the diffusion coefficient. Moreover, an increase in temperature results in fracture cleavage and the formation of voids in the product layer. These structural changes facilitate penetration of the selenium melt through the product layer to the reaction interface, thereby enhancing the erosion rate.

The reaction time clearly affects the erosion rate of PbTe particle in selenium melt. Generally, the leaching rate gradually decreases with increasing reaction time for a leaching reaction that involves the generation of a solid product layer [20,21] because the solid product layer, which encases the reactants, impedes diffusion of the solution toward the reaction interface. The results

presented in Fig. 7 demonstrate that the selenium melt erodes the PbTe particles more slowly with increasing reaction time at temperatures of 573, 583, and 593 K, consistent with the above-mentioned general leaching trend. However, different patterns are observed at 603 and 613 K: the erosion rate initially decreases within the first 30 min, and then begins to accelerate as the reaction time increases further. This behavior is attributable to the appearance of voids within the broken and cracked product layers; these voids facilitate the penetration of the selenium melt through the product layer, enabling it to reach the reaction interface more easily, thereby enhancing the erosion rate as a consequence.

3.2 PbTe erosion kinetics in selenium melt

Figure 8 shows the PbTe particle diffusion process during erosion in the selenium melt based on the unreacted core shrinkage model [22−24]. The limiting steps of the reaction include: (1) external diffusion of the liquid Se reactant or Te product through the liquid boundary layer, (2) inward diffusion of the liquid Se reactant or Te product through the solid product layer, and (3) the interfacial chemical reaction between Se and PbTe. In Fig. 8, r is the radius of the PbTe sample at any time (mm), r_0 is the original radius of the PbTe sample (mm), r_1 ($=r_0+\sigma$) is the thickness of the liquid boundary layer (mm), $C_{\mathrm{PbTe}}^{\mathrm{Te(Se)}}$ is the concentration of Te(Se) in the reactant at the interface between the product layer and PbTe sample (g/mm^3), $C_{\mathrm{PbSe}}^{\mathrm{Te(Se)}}$ is the concentration of Te(Se) in the reaction product at the interface between the product layer and PbTe sample (g/mm^3), $C_{\mathrm{Te(Se)}}^{*}$ is the concentration of Te(Se) in the boundary layer at the interface between the product and boundary layers (g/mm^3), and $C_{\mathrm{Te(Se)}}$ is the concentration of Te(Se) in the selenium melt (g/mm^3).

According to the unreacted core shrinkage model, the limiting steps involved in the PbTe particle erosion process for a cylindrical sample in selenium melt include interfacial chemical reaction, diffusion of the product layer, and diffusion control involving the boundary layer [25]. Here, r is proportional to the reaction time (t) when the limiting step is an interfacial chemical reaction, while $r^2+2r^2\ln r_0-2r^2\ln r$ is proportional to t when the limiting step is a product-layer diffusion process. On the other hand, r^2 is proportional to t when the limiting step is a mass-transfer process in the boundary layer. The abovementioned processes are represented by Eqs. (4)−(6), respectively:

$$r = r_0 - \frac{1}{\rho_{\mathrm{PbTe}}}\cdot\left(C - C_{\mathrm{Te}}\right)\cdot k_{\mathrm{r}}\cdot t \tag{4}$$

$$r^2 + 2r^2\ln r_0 - 2r^2\ln r = 2{r_0}^2\ln r_0 + {r_0}^2 - \frac{4}{\rho_{\mathrm{PbTe}}}\cdot\left(C - C_{\mathrm{Te}}\right)\cdot D_{\mathrm{s}}\cdot t \tag{5}$$

$$r^2 = {r_0}^2 - \frac{2}{\rho_{\mathrm{PbTe}}}\cdot\left(C - C_{\mathrm{Te}}\right)\cdot D_{\mathrm{l}}\cdot\frac{1}{\ln r_{\mathrm{l}} - \ln r_0}\cdot t \tag{6}$$

where $C(=C_{\mathrm{PbTe}}^{\mathrm{Te}}+C_{\mathrm{PbSe}}^{\mathrm{Te}})$ is considered the total amount of free Te at the interface between the product layer and the PbTe sample (g/mm^3), ρ_{PbTe} is the density of PbTe particles (g/mm^3), t is the reaction time (s), k_{r} is the rate constant of the interfacial chemical reaction, D_{s} is the diffusion constant (mm/s), and D_{l} is the effective diffusion coefficient for Te through the liquid boundary layer (mm/s).

The experiments involving PbTe particles immersed in selenium melt at various temperatures were used to investigate the limiting step of the reaction. Linear fitting was used to correlate the thickness of the product layer with the reaction time at various temperatures, as presented in Fig. 9.

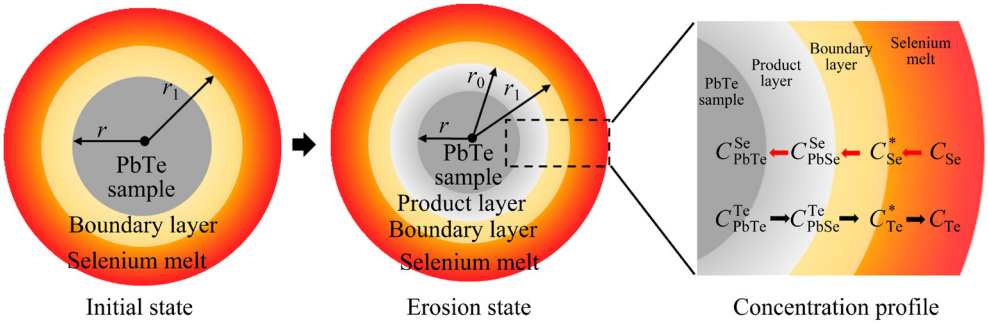

Fig. 8 Schematic diagram of PbTe particle erosion process in selenium melt

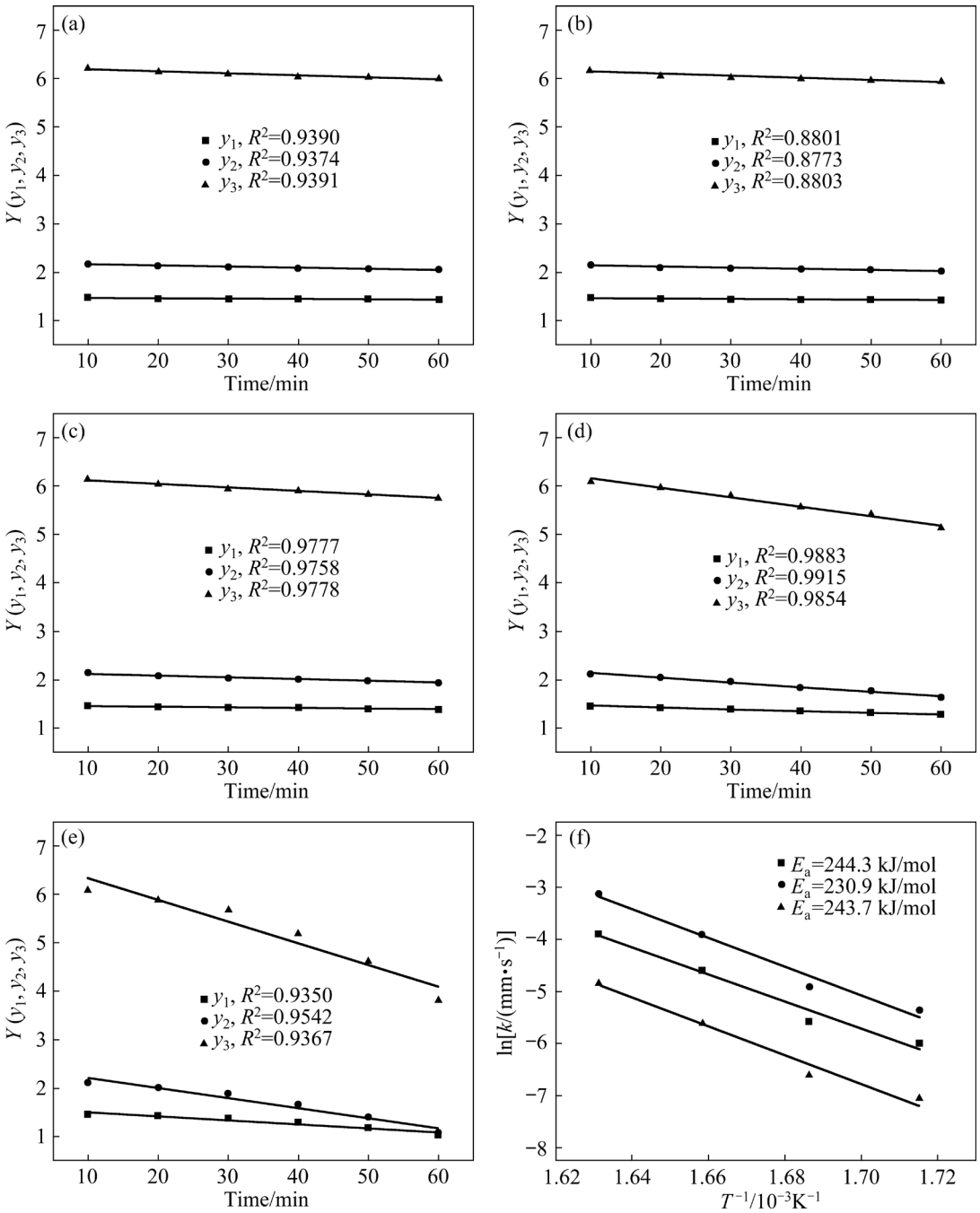

Fig. 9 Relationships between y and t under varying temperatures during erosion of PbTe particles in selenium melt at (a) 573 K, (b) 583 K, (c) 593 K, (d) 603 K, and (e) 613 K; (f) Illustrative plots of ln k vs 1/T

Figures 9(a−e) show the experimental data and fitted linear relationships for reactions conducted at 573, 583, 593, 603, and 613 K, respectively. The results reveal that the strongest linear relationship exists between y_3 (r^2+2r^2ln r_0−2r^2ln r) and t and between y_1 (r) and t at 573, 583, and 593 K, suggesting that erosion of the PbTe particle in the selenium melt is simultaneously controlled by intra-layer diffusion and interfacial chemical reactions at lower reaction temperatures. The strongest linear relationship is observed between y_2 (r^2) and t at higher temperatures of 603 and 613 K, which indicates that diffusion within the boundary layer is the dominant factor controlling the PbTe particle erosion rate under these conditions.

Furthermore, activation energy is determined by plotting ln k vs 1/T according to the Arrhenius equation (Eq. (7)):

$$k = k_0 \exp\left(-\frac{E_a}{RT}\right) \quad (7)$$

where k is the total kinetic rate constant, k_0 is the frequency factor, E_a is the apparent activation energy, and R is the molar gas constant.

Figure 9(f) shows that activation energy for PbTe particle erosion in the selenium melt is 244.3 kJ/mol when the reaction is controlled by diffusion within the product layer and interfacial chemical reactions. Conversely, the corresponding activation energy is 230.9 kJ/mol when the reaction is regulated by diffusion within the boundary layer.

3.3 Mechanism analysis

The overall reaction process is shown in Fig. 10. Initially, the Se in the selenium melt reacts with PbTe at the reaction interface through the liquid boundary layer, resulting in the formation of PbSe and Te. PbSe then encapsulates the inner PbTe layer as a solid product layer. Because Te and Se are infinitely mutually soluble, the generated Te diffuses into the selenium melt through the boundary layer, and the Se subsequently reaches the reaction interface by traversing both the boundary and solid product layers, where it continues to react with the unreacted PbTe core. At the same time, the Te produced during this reaction diffuses into the selenium melt through both the product and boundary layers.

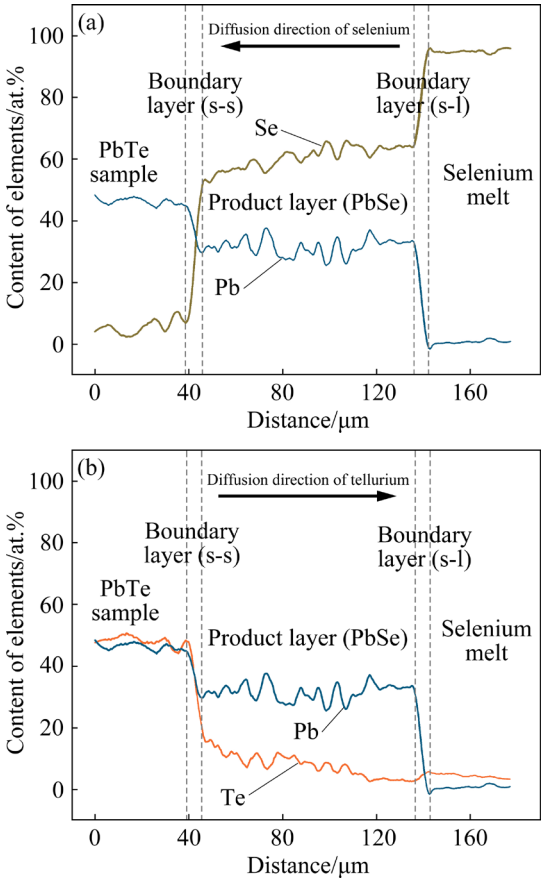

Fig. 10 Schematic showing concentration distributions of diffused (a) Se and (b) Te at various interfaces

As the reaction progresses, the reaction products continuously generated on the PbTe particle surface increase the thickness of the reaction product layer, thus hampering the diffusion of Se into the reaction interface through the product layer. This impedes the further generation of reaction products to some extent and thus partially blocks the erosion process. The erosion rate decreases with increasing reaction time at lower temperatures (573, 583, and 593 K), and diffusion of the product layer becomes the limiting factor for the erosion process. Specifically, as the interfacial chemical reaction proceeds, the consumption of Se atoms at the reaction interface becomes comparable to the number of Se atoms arriving at the reaction interface via diffusive migration. The rates of the interfacial chemical reaction and Se atom entry via diffusion exhibit minimal differences; consequently, product-layer diffusion becomes the limiting step during the erosion of PbTe by selenium. Hence, the erosion of PbTe by Se is concurrently controlled by the diffusion of the product layer and the interfacial chemical reaction. However, the rate of interfacial chemical reaction is observed to accelerate with time at higher temperatures (603 and 613 K). In addition, increasing the temperature results in crack formation and the appearance of voids in the product layer, which enable the Se in the melt to access the reaction interface through diffusion within the product layer. Consequently, the diffusion of the product layer no longer limits the PbTe particle erosion by selenium; instead, the limiting step of the reaction becomes the diffusion within the boundary layer.

Diffusion of the reaction product (i.e., Te) into the selenium melt during this process occurs through the solid product layer. Te atoms generated within the product layer diffuse according to the Kirkendall effect because both PbSe and Te are solid reaction products at the reaction temperature [26,27], as depicted in Fig. 11. The rate of Se atom diffusion toward the reaction interface decreases as the reaction product layer thickens. However, Te atoms within the product layer diffuse according to

the Kirkendall effect, with minimal change in the rate at which the Te atoms generated by the reaction enter the selenium melt through diffusion.

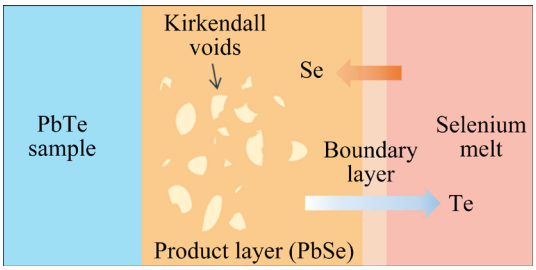

Fig. 11 Diagram of diffusion mechanism involving Se and Te in product layer

In the initial stages of the reaction, which are characterized by a solid product layer thickness below the critical value of 110 μm, the disparity between the rates of Se atom transport through the product layer and Te atom migration into the selenium melt via the product layer is insignificant. At this point, the solid product layer exists in a state of dynamic equilibrium with respect to atomic diffusion. In the later stages of the reaction (once the thickness of the solid product layer exceeds the critical threshold of 110 μm), the rate at which Se atoms reach the reaction interface through the product layer is slower than the rate at which Te atoms enter the selenium melt via the product layer. This discrepancy stems from an imbalance in diffusion coupling between the Se and Te atoms through the reaction product layer. Macroscopically, this imbalance manifests as cavities within the product layer that are generated by the Te atoms formed during the reaction and remain unfilled by Se atoms, thereby creating vacancies at the atomic level; collectively, these holes give rise to Kirkendall voids within the product layer. This phenomenon explains the appearance of voids within the product layer during extended reaction times and at higher temperatures (603 and 613 K), as the Kirkendall effect is accelerated with increasing temperature.

4 Conclusions

(1) At lower temperatures (573, 583, and 593 K), the PbTe particle erosion rate in the selenium melt is controlled by both diffusion through the product layer and the interfacial chemical reaction; the activation energy for the reaction is 244.3 kJ/mol. However, the PbTe particle erosion rate at higher temperatures (603 and 613 K) is primarily governed by diffusion through the boundary layer; the activation energy for this reaction is 230.9 kJ/mol.

(2) Atomic diffusion within the solid product layer follows the Kirkendall effect; as the product layer thickens, the rate at which Te atoms generated by the reaction diffuse into the selenium melt through the product layer is significantly higher than that at which Se atoms diffuse through the product layer to reach the reaction interface. This disparity in diffusion rates leads to the formation of Kirkendall voids within the product layer owing to the imbalance in atomic diffusion.

(3) PbTe impurity particles react with Se to form PbSe particles and Te in the selenium melt, and the Te formed by the reaction is evenly distributed in the selenium melt because Te and Se are infinitely miscible. This study provides a rationale for the inability to completely remove Te impurities during Se purification via vacuum distillation.

CRediT authorship contribution statement

Lang LIU: Methodology, Formal analysis, Investigation, Writing − Original draft, Visualization; **Xian-jun LEI** and **Huan LUO:** Data curation, Writing − Review & editing; **Guo-zheng ZHA:** Writing − Review & editing; **Ru-yi JI:** Formal analysis, Writing – Review & editing; **Ji-lin HE, Wen-long JIANG** and **Bin YANG:** Resources, Writing − Review & editing; **Bao-qiang XU:** Supervision, Project administration, Funding acquisition.

Declaration of competing interest

The authors declare that they have no known competing financial interests or personal relationships that could have appeared to influence the work reported in this paper.

Acknowledgments

The authors would like to express their sincere thanks to the National Key Research and Development Program of China (No. 2022YFC2904900), and the National Natural Science Foundation of China (No. U1902221).

References

[1] YU C C, WU H, DENG P Y, AGNE M T, SNYDER G J, CHU J P. Thin-film metallic glass: An effective diffusion barrier for Se-doped $AgSbTe_2$ thermoelectric modules [J]. Scientific Reports, 2017, 7(1): 45177.

[2] LI Zhi-qiang, CHEN Xu, ZHU Hong-bing, CHEN Jing-wei, GUO Yu-ting, ZHANG Chong, ZHANG Wen, NIU Xiao-na, MAI Yao-hua. Sb_2Se_3 thin film solar cells in substrate configuration and the back contact selenization [J]. Solar Energy Materials and Solar Cells, 2017, 161: 190−196.

[3] HASSANIEN A S, AKL A A. Effect of Se addition on optical and electrical properties of chalcogenide CdSSe thin films [J]. Superlattices and Microstructures, 2016, 89: 153−169.

[4] CHEN Wan-wen, LI Xiao-jiao, CHENG Hao, XIA Wen-shui. Chitosan-based selenium composites as potent Se supplements: Synthesis, beneficial health effects, and applications in food and agriculture [J]. Trends in Food Science & Technology, 2022, 129: 339−352.

[5] LIAMPAS A, ZIS P, HADJIGEORGIOU G, VAVOUGIOS G D. Selenium, stroke, and infection: A threefold relationship; Where do we stand and where do we Go? [J]. Nutrients, 2023, 15(6): 1405.

[6] ZENG Yan-liang, ZOU Jian-bo, LIAO Chun-fa, LIU Fu-peng, ZHOU Xun. Selective separation and recovery of selenium from copper anode slime by compound leaching followed by sulfate roasting [J]. Minerals Engineering, 2022, 186: 107749.

[7] LUO Huan, JIANG Wen-long, ZHA Guo-zheng, LIU Lang, ZHEN Tian-tian, YANG Bin, XU Bao-qiang. Removal of impurity Pb during crude selenium purification by controlling potential oxidation and vacuum distillation [J]. Vacuum, 2022, 195: 110674.

[8] XU Bin, CHEN Yan-zhu, DONG Zhong-lin, JIANG Tao, ZHANG Bang-sheng, LIU Gui-qing, YANG Jun-kui, LI Qian, YANG Yong-bin. Eco-friendly and efficient extraction of valuable elements from copper anode mud using an integrated pyro-hydrometallurgical process [J]. Resources, Conservation and Recycling, 2021, 164: 105195.

[9] RAO Shuai, LIU Yi, WANG Dong-xing, CAO Hong-yang, ZHU Wei, YANG Rui, DUAN Li-juan, LIU Zhi-qiang. Pressure leaching of selenium and tellurium from scrap copper anode slimes in sulfuric acid-oxygen media [J]. Journal of Cleaner Production, 2021, 278: 123989.

[10] YANG Hong-ying, LI Xue-jiao, TONG Lin-lin, JIN Zhe-nan, YIN Lu, CHEN Guo-bao. Leaching kinetics of selenium from copper anode slimes by nitric acid-sulfuric acid mixture [J]. Transactions of Nonferrous Metals Society of China, 2018, 28(1): 186−192.

[11] SINES I T, SCHAAK R E. Phase-selective chemical extraction of selenium and sulfur from nanoscale metal chalcogenides: A general strategy for synthesis, purification, and phase targeting [J]. Journal of the American Chemical Society, 2011, 133(5): 1294−1297.

[12] KONG Xiang-feng, YANG Bin, XIONG Heng, KONG Ling-xin, LIU Da-chun, XU Bao-qiang. Thermodynamics of removing impurities from crude lead by vacuum distillation refining [J]. Transactions of Nonferrous Metals Society of China, 2014, 24(6): 1946−1950.

[13] MEI Qing-song, ZHA Guo-zheng, LIU Da-chun, YANG Bin, JIANG Wen-long. A study on purifying selenium and enriching gold and silver by vacuum distillation [J]. Journal of Kunming University of Science and Technology. 2018, 43: 14−21. (in Chinese)

[14] ZHA Guo-zheng, Wang Yun-ke, CHENG Min-qiang, HUANG Da-xin, JIANG Wen-long, XU Bao-qiang, YANG Bin. Purification of crude selenium by vacuum distillation and analysis [J]. Journal of Materials Research and Technology. 2020, 9(3): 2926−2933.

[15] ZHA Guo-zheng, KONG Xiang-feng, JIANG Wen-long, YANG Bin, XU Bao-qiang, LIU Da-chun, MEI Qing-song, CHEN Wei. Sustainable chemical reaction-free vacuum separation process to extract selenium from high-value-added hazardous selenium sludge [J]. Journal of Cleaner Production. 2020, 275(2): 124083.

[16] VOLODIN V N, TREBUKHOV S A, BURABAEVA N M, NITSENKO A V. Melt–gas phase equilibria and state diagrams of the selenium–tellurium system [J]. Russian Journal of Physical Chemistry A, 2017, 91(5): 800−804.

[17] LUO Huan, XIONG Heng, JIANG Wen-long, LIU Lang, ZHA Guo-zheng, ZHEN Tian-tian, YANG Bin, XU Bao-qiang. Theoretical analysis and experimental verification of thermal decomposition mechanism of CuSe [J]. Transactions of Nonferrous Metals Society of China, 2022, 32(10): 3478−3486.

[18] EDEARD J T. Molecular volumes and the Stokes-Einstein equation [J]. Journal of Chemical Education, 1970, 47(4): 261.

[19] REN Zhong-shan, HU Xiao-jun, HOU Xin-mei, XUE Xiang-xin, CHOU Kuo-chih. Dissolution and diffusion of TiO_2 in the $CaO−Al_2O_3−SiO_2$ slag [J]. International Journal of Minerals, Metallurgy, and Materials, 2014, 21: 345−352.

[20] CAO Rui-lin, JIA Zi-jian, ZHANG Zu-hua, ZHANG Ya-mei, BANTHIA N. Leaching kinetics and reactivity evaluation of ferronickel slag in alkaline conditions [J]. Cement and Concrete Research, 2020, 137: 106202.

[21] SHI Gong-chu, LIAO Ya-long, SU Bo-wen, ZHANG Yu, WANG Wei, XI Jia-jun. Kinetics of copper extraction from copper smelting slag by pressure oxidative leaching with sulfuric acid [J]. Separation and Purification Technology, 2020, 241: 116699.

[22] KHAWAM A, FLANAGAN D R. Solid-state kinetic models: Basics and mathematical fundamentals [J]. The Journal of Physical Chemistry B, 2006, 110(35): 17315−17328.

[23] TRIPATHI G, MALFIET A, BLANPAIN B, GUO M X. Kinetic aspects of aluminum oxide dissolution in molten BOF slag [J]. Metallurgical and Materials Transactions B, 2021, 52: 1614−1625.

[24] UM H, YEO S, KANG Y B, CHUNG Y. The effect of Fe_xO content on dissolution behavior of an alumina inclusion in $CaO−Al_2O_3−SiO_2−Fe_xO$ slag by a single hot thermocouple technique [J]. Ceramics International, 2022, 48(23): 35301−35309.

[25] LI Zhi-rong, JIA Bo-ran, ZHANG Ya-bing, HE Sheng-ping, WANG Qiang-qiang, WANG Qian. Dissolution behaviour of Al_2O_3 in mould fluxes with low SiO_2 content [J]. Ceramics International, 2019, 45(3): 4035−4042.

[26] ZHANG Fan, ZHANG Bo-yan, CHEN Xiao-pan, ZHANG Xin-hong, ZHU Xiao-ke, DU Hai-shun. Computational simulation of voids formation and evolution in Kirkendall effect [J]. Physica A: Statistical Mechanics and its Applications, 2020, 554: 124285.

[27] GUO Hu-cheng, RAO Mei, ZHANG Jian, WANG Xue-fei, LUO Guo-qiang, SHEN Qiang. Electromigration-enhanced Kirkendall effect of Cu/Ti direct diffusion welding by sparking plasma sintering [J]. Journal of Materials Processing Technology, 2023, 315: 117933.

PbTe 在硒熔体中的侵蚀和扩散动力学

刘 浪[1,2,3]，何季麟[4]，雷现军[1,2,3,5]，罗 欢[1,2,3]，
查国正[1,2,3,5]，戢如意[6]，蒋文龙[1,2,3,5]，杨 斌[1,2,3,5]，徐宝强[1,2,3,5]

1. 昆明理工大学 云南省有色金属真空冶金重点实验室，昆明 650093；
2. 昆明理工大学 真空冶金国家工程研究中心，昆明 650093；
3. 昆明理工大学 冶金与能源工程学院，昆明 650093；
4. 郑州大学 材料科学与工程学院，郑州 450001；
5. 昆明理工大学 省部共建复杂有色金属资源清洁利用国家重点实验室，昆明 650093；
6. 四川大学 材料科学与工程学院，成都 610064

摘 要：研究了 PbTe 颗粒在硒熔体中的侵蚀过程，并对该过程的动力学进行了分析。结果表明，在较低温度(573、583 和 593 K)下，PbTe 颗粒的侵蚀过程主要受产物层扩散和界面化学反应控制，在较高温(603 和 613 K)下则受边界层扩散控制。随着产物层的加厚，硒、碲原子在产物层中的扩散变得不平衡，导致产生柯肯达尔孔洞，加速 PbTe 颗粒的侵蚀过程。硒熔体中的杂质 PbTe 演变成 PbSe 和 Te 后，由于硒、碲同族相溶性，碲均匀分布在硒熔体中。该研究阐明了杂质 PbTe 在硒熔体中的演化行为以及导致碲常赋存于硒中的原因。

关键词：碲化铅；硒；扩散动力学；侵蚀行为

(Edited by Bing YANG)